Earth and Planetary Science Letters 293 (2010) 289–299

Contents lists available at ScienceDirect

Earth and Planetary Science Letters

journal homepage: www.elsevier.com/locate/epsl

Poroelastic stress-triggering of the 2005 M8.7 Nias earthquake by the 2004 M9.2 Sumatra–Andaman earthquake

Kristin L.H. Hughes [a,*], Timothy Masterlark [a], Walter D. Mooney [b]

[a] University of Alabama, 201 7th Avenue, Tuscaloosa, AL 35487, USA
[b] U.S. Geological Survey, Menlo Park, CA 94025, USA

ARTICLE INFO

Article history:
Received 2 October 2009
Received in revised form 22 February 2010
Accepted 25 February 2010
Available online 23 March 2010

Editor: L. Stixrude

Keywords:
Sumatra–Andaman earthquake
Nias earthquake
poroelastic mechanics
earthquake triggering
finite element models

ABSTRACT

The M9.2 Sumatra–Andaman earthquake (SAE) occurred three months prior to the M8.7 Nias earthquake (NE). We propose that the NE was mechanically triggered by the SAE, and that poroelastic effects were a major component of this triggering. This study uses 3D finite element models (FEMs) of the Sumatra–Andaman subduction zone (SASZ) to predict the deformation, stress, and pore pressure fields of the SAE. The coseismic slip distribution for the SAE is calibrated to near-field GPS data using FEM-generated Green's Functions and linear inverse methods. The calibrated FEM is then used to predict the postseismic poroelastic contribution to stress-triggering along the rupture surface of the NE, which is adjacent to the southern margin of the SAE. The coseismic deformation of the SAE, combined with the rheologic configuration of the SASZ produces two transient fluid flow regimes having separate time constants. SAE coseismic pore pressures in the relatively shallow forearc and volcanic arc regions (within a few km depth) dissipate within one month after the SAE. However, pore pressures in the oceanic crust of the down-going slab persist several months after the SAE. Predictions suggest that the SAE initially induced MPa-scale negative pore pressure near the hypocenter of the NE. This pore pressure slowly recovered (increased) during the three-month interval separating the SAE and NE due to lateral migration of pore fluids, driven by coseismic pressure gradients, within the subducting oceanic crust. Because pore pressure is a fundamental component of Coulomb stress, the MPa-scale increase in pore pressure significantly decreased stability of the NE fault during the three-month interval after the SAE and prior to rupture of the NE. A complete analysis of stress-triggering due to the SAE must include a poroelastic component. Failure to include poroelastic mechanics will lead to an incomplete model that cannot account for the time interval between the SAE and NE. Our transient poroelastic model explains both the spatial and temporal characteristics of triggering of the NE by the SAE.

1. Introduction

In northern Indonesia, the Indo-Australian plate obliquely subducts beneath the Burma microplate and Sunda plate. The complex tectonic setting transitions from oblique subduction off the west coast of Sumatra to almost complete right-lateral strike-slip motion near the Andaman and Nicobar Islands to the north (Fig. 1) (Bird, 2003). The 26 December 2004 Sumatra–Andaman earthquake (SAE) ruptured over 1200 km of the Indo-Australian and Burma plate boundary (Ammon et al., 2005; Bilek, 2007; Vigny et al., 2005). Three months later, the 28 March 2005 Nias earthquake (NE) ruptured about 400 km of the same plate boundary immediately to the south of the SAE rupture (Ammon et al., 2005; Banerjee et al., 2007).

The southern boundary of the SAE rupture is thus a seismic barrier that divides slip on the megathrust into the northern Sumatra–Andaman and southern Nias segments (Fig. 1) (Ammon et al., 2005). The physical cause of this seismic barrier is likely due to a change in the seafloor morphology, associated with the northern extent of a series of prominent offshore islands that are the result of the uplift of the seafloor above the subducting oceanic ridge. The subduction of the extinct oceanic ridge may have caused a permanent kink in the subducting slab, which has been imaged by Pesicek et al. (2008). The seismic barrier also corresponds to a pronounced bend in the geometry of the oceanic trench at the toe of the megathrust (Fig. 1). Ridge subduction creates seismic barriers in numerous subduction zones worldwide (Gutscher et al., 1999; Ruff, 1996). The subduction of the Chile Rise at the southern terminus of the 1960 $M_w = 9.5$ megathrust earthquake is one example (Plafker and Savage, 1970). Seismic barriers may also correspond to changes in the coupling between the overriding plate and the subducting oceanic lithosphere at the megathrust due to the thinner sediment load above the subducting ridge. Seismic barriers thus correspond to a pronounced change in physical properties along the megathrust.

* Corresponding author.
E-mail addresses: klhhughes@gmail.com (K.L.H. Hughes), masterlark@ua.edu (T. Masterlark), mooney@usgs.gov (W.D. Mooney).

0012-821X/$ – see front matter © 2010 Elsevier B.V. All rights reserved.
doi:10.1016/j.epsl.2010.02.043

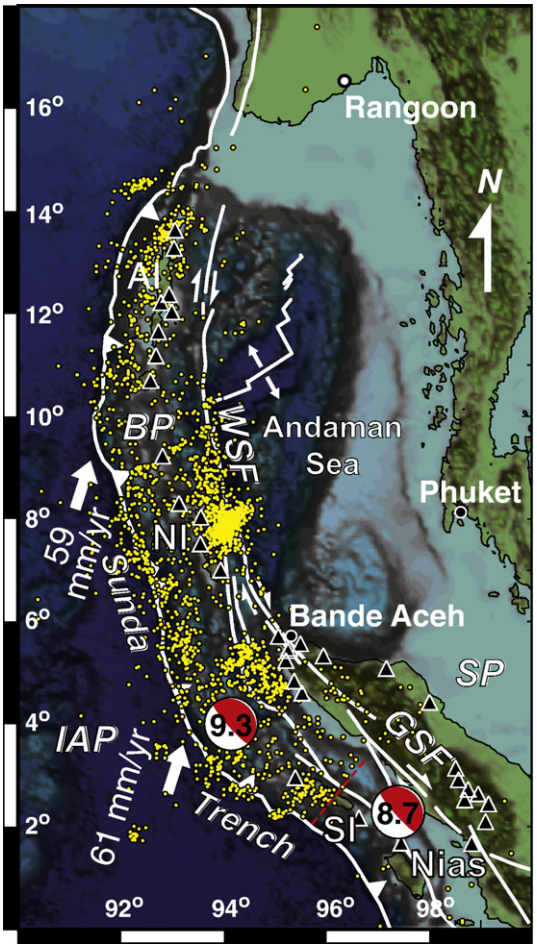

Fig. 1. Seismotectonic setting of the SAE (adapted from Masterlark and Hughes (2008)). Harvard CMT Focal mechanisms are given for the 26 December 2004 (M9.2) and 28 March 2005 (M8.7) earthquakes. Aftershock epicenters (yellow dots), spanning 26 December 2004 through 28 March 2005, illuminate the surface projection of the M9.2 rupture (http://neic.usgs.gov). The rupture initiated on the southeast portion of the fault and propagated 1200 km northward. The sharply truncated aftershock distribution, shown with a NE-trending dashed line that bisects Simeulue Island, marks the boundary between rupture of the M9.2 and subsequent M8.7 events (seismic barrier). Black triangles are near-field GPS sites (Gahalaut et al., 2006; Subarya et al., 2006). The tectonic configuration is modified from Bird (2003) and overlies a shaded relief image of global relief data (http://www.ngdc.noaa.gov). Abbreviations are Andaman Islands (AI), Burma Plate (BP), Indo-Australian Plate (IAP), Nicobar Islands (NI), Simeulue Island (SI), Great Sumatran Fault (GSF), Sunda Plate (SP), and West Sumatra Fault (WSF).

The coseismic and postseismic deformation of the SAE changed the stress regime of the Sumatra–Andaman subduction zone (SASZ). We propose that the M8.7 NE was triggered by the M9.2 SAE, based on the proximity of these two great earthquakes in both space and time. Previous stress-triggering analyses of the SAE predict that the SAE increased the Coulomb stress near the hypocenter of the NE (Gahalaut and Kalpna, 2005; McCloskey et al., 2005). However, neither of these analyses included a transient mechanism to account for the three-month interval separating the SAE and NE. Others suggest transient mechanisms, such as postseismic viscoelastic relaxation and afterslip, impose time-dependence on the Coulomb stress, which thereby increases during the three-month interval between earthquakes and advanced the occurrence of the NE (Hsu et al., 2006; Mignan et al., 2006; Pollitz et al., 2006a). However, none of these previous analyses account for the pore pressure effects, which are known to significantly influence Coulomb stress calculations over time periods consistent with the separation of the SAE and NE events (Beeler et al., 2000; Masterlark, 2003; Masterlark and Wang, 2000; Masterlark and Wang, 2002). We construct poroelastic deformation models of the SAE to test the hypothesis that pore fluid pressure near the hypocenter of the NE continually increased during the three-month interval separating the SAE and NE. This increasing pore pressure translates to increasing Coulomb stress and thus predicts a systematic decrease in fault stability leading to the rupture of the NE.

2. Methods

2.1. Coulomb stress

Stress-triggering is a mechanism for which a loading event, such as slip along a fault, changes the frictional stability of other faults in the near-field region. Coulomb stress calculations allow us to quantify the changes in tendency for frictional slip to occur along a locked, pre-existing fault. The change in Coulomb stress (σ_c) for a given fault is

$$\sigma_c = \sigma_s + f(\sigma_n + P) \quad (1)$$

where σ_s is shear stress parallel to a specified slip vector, σ_n is fault-normal stress (tension-positive), P is pore pressure, and f is the coefficient of friction (e.g., King et al., 1994; Masterlark and Wang, 2000). Positive values of the change in Coulomb stress indicate an increased tendency for the fault to slip and negative values indicate increased stability. We assume that the state variables σ and P are incremental changes with respect to a reference state.

Fault-slip from an earthquake induces relatively instantaneous incremental changes in stress and pore pressure in the near-field region, while afterslip, poroelastic effects, viscoelastic relaxation, and interseismic strain accumulation drive transient changes in stress and pore pressure after an earthquake has occurred. Static (vis-à-vis quasi-static) stress-triggering analyses of the causal relationship between earthquakes are applicable for either short times (undrained conditions, negligible viscous relaxation) or long times (drained conditions, negligible deviatoric stresses in the viscous material) following a dislocation (Wang, 2000). Undrained or drained conditions imply either fluid-flux equals zero or pore pressure equals zero, respectively. Laboratory experiments on a variety of rocks indicate that the coefficient of friction is robust and lies between 0.65 and 0.85 (Byerlee, 1978).

Alternatively, changes in Coulomb stress are often calculated using the assumption that pore-pressure is proportional to the fault-normal stress rather than the mean-normal stress used in standard poroelastic theory (e.g., King et al., 1994; Stein, 1999). In this case, Eq. (1) is modified to

$$\sigma_c = \sigma_s + f'\sigma_n \quad (2)$$

where f' is an *apparent* coefficient of friction that is some unknown combination of material properties and transient fluid-flow conditions (Masterlark and Wang, 2000), such that f' is theoretically unbounded ($-\infty < f' < \infty$) (Beeler et al., 2000). The assumption that pore-fluid pressure is proportional to fault-normal stress alone holds only if the fault zone is relatively compliant with respect to the surrounding materials (Cocco and Rice, 2002; Cocco and Rice, 2003). However, because Coulomb stress is often calculated for regions saturated with aftershocks along multiple faults (rather than a single fault), a problem domain including compliant fault zones no longer satisfies the homogeneous assumption required by standard analytical models for displacement due to an elastic dislocation (e.g., Okada, 1992). This problem can be extended to models that simulate distributions of material properties that do not include weak fault zones (Chlieh et al., 2007; Hsu et al., 2006; Masterlark and Hughes, 2008). Because of these contradictory assumptions, Eq. (2) leads to important prediction errors (Beeler et al., 2000; Masterlark, 2003; Masterlark and Wang, 2000).

2.2. Deformation model

Deformation models provide the linkage between the observed surface deformation and the source of the deformation—the fault-slip at depth. While forward models allow us to predict deformation caused by fault-slip, inverse models estimate the distribution of fault-slip, based on observed deformation and pre-supposed deformation models. To delimit the geometry of the rupture surface, we can use geodetic or seismic data. In both cases, a model and some assumptions are required. For the SAE, the location of the rupture is constrained by seismicity (Fig. 1), seismogenic data (Ammon et al., 2005; Stein and Okal, 2005), and results from previous modeling studies (Chlieh et al., 2007; Hughes and Masterlark, 2008; Masterlark and Hughes, 2008).

The 3D finite element model (FEM) presented in this study is designed to simulate coseismic and poroelastic postseismic deformation of the SAE, while simultaneously accounting for the known geologic structure of the subduction zone. We use the general-purpose FEM code Abaqus (http://www.simulia.com) to solve for displacement (u) and coupled displacement and pore-fluid pressure (u, P) over a 3D problem domain partitioned into elastic and poroelastic regions, respectively. The FEM is driven by a coseismic slip distribution calibrated to near-field GPS data. Rather than use a published slip distribution for the SAE, we calibrate the slip distribution via least-squares inverse methods that account for the distribution of material properties within the 3D problem domain of the FEM. Expressed in index notation, the governing equations for poroelastic materials are

$$G\nabla^2 u_i + \frac{G}{(1-2\nu)}\frac{\partial^2 u_k}{\partial x_i \partial x_k} = \alpha\frac{\partial P}{\partial x_i} - F_i \tag{3}$$

$$\alpha\frac{\partial \varepsilon_{kk}}{\partial t} + S_\varepsilon\frac{\partial P}{\partial t} = \frac{\kappa}{\mu_f}\nabla^2 P + Q \tag{4}$$

where G is the shear modulus, ν is Poisson's ratio (drained), α is the Biot–Willis coefficient, F is a body force per unit volume, $\varepsilon_{kk} = \Sigma \partial u_k/\partial x_k$ is the volumetric strain, S_ε is the constrained storage coefficient, κ is the permeability coefficient, and μ_f is the pore-fluid viscosity, and Q is a fluid source term defined as volume of fluid per unit bulk volume per unit time (Wang, 2000). The subscript i spans orthogonal direction components 1, 2, and 3 and the subscript k implies summation over these three components. In this formulation, x_1, x_2, and x_3 are equivalent Cartesian coordinates x, y, and z (east, north, and vertical), respectively. Similarly, u_1, u_2, and u_3 are equivalent to u_x, u_y, and u_z, respectively. Viscoelastic behavior in the mantle is simulated by imposing an additional stress-dependent creep relationship. The total longitudinal equivalent strain is:

$$\varepsilon = \varepsilon_e + \varepsilon_f \text{ and } \frac{d\varepsilon_f}{dt} = A\sigma_d^\eta \tag{5}$$

where ε_e is the elastic strain, ε_f is the strain due to viscous flow, A is a constant that can be augmented to account for temperature dependence, and σ_d is the deviatoric stress. The relationship is equivalent to a Maxwell material for $\eta = 1$ and A is half of the inverse of the linear viscosity (Turcotte and Schubert, 2002).

The governing equations for an elastic material are recovered from Eqs. (3), (4), and (5) by setting $P = 0$ and assuming steady-state conditions, with all time derivatives equal to zero. The governing equations for elastic materials are sufficient to describe limiting cases of drained (long time; $P = 0$) and undrained (short time; no fluid flow) static deformation, by substituting drained and undrained values of Poisson's ratios, respectively. However, a description of transient poroelastic deformation requires both Eqs. (3) and (4) (Wang, 2000).

2.3. FEM configuration

Construction of the SAE FEM involves a series of steps. First, we design a trench-normal slice through the SASZ (Fig. 2). The fault-slip of the SAE occurs along the interface separating the subducting slab, consisting of depleted mantle capped by mid-oceanic ridge basalt (MORB), and the overriding forearc (Kopp and Kukowski, 2003; Kopp et al., 2002) and enriched mantle wedge (Kieckhefer et al., 1980; Kopp et al., 2002; Kopp and Kukowski, 2003). Seismicity data (Engdahl et al., 2007) constrain the geometry of the subducting slab. The configurations of the volcanic arc and backarc basin regions are based on geologic maps and cross-sections of the SASZ (Barber et al., 2005).

Second, we sweep this two-dimensional cross section along the curving strike of the Sunda trench to produce a three-dimensional model (Fig. 2). This configuration implicitly assumes the geologic structure is constant along the trench. The tessellated problem domain comprises about 340,000 octahedral finite elements having trilinear interpolation basis functions and 1,000,000 degrees of freedom. The characteristic dimension for elements is a few kilometers near the fault and generally increases with distance from the fault. This tessellation is validated by Masterlark and Hughes (2008).

Third, we specify a distribution of rheologic properties over the partitioned problem domain (Fig. 2). The elastic and poroelastic properties are taken from compilations of laboratory experiments (Turcotte and Schubert, 2002; Wang, 2000). The elastic properties are in accord with seismic tomography and gravity data (Kieckhefer et al., 1980; Kopp et al., 2002; Kopp and Kukowski, 2003). This configuration is similar to that of Masterlark and Hughes (2008) and includes both lateral and vertical rheologic variations that correspond to the regional-scale geologic structure of a subduction zone. The viscoelastic rheology is specified for the mantle only in a separate FEM used to predict long-term postseismic deformation discussed later.

Fourth, we specify boundary conditions and impose fault-slip. The far-field lateral boundaries and base of the problem domain are zero displacement. The top of the problem domain is a stress-free surface. The subducting slab and overriding plate are welded together along the intersection of the fault and the trench. Quasi-static fault-slip can be simulated with an FEM as the dislocation of a node-pair, implemented via kinematic constraint equations (Masterlark, 2003; Masterlark and Hughes, 2008; Melosh and Raefsky, 1981; Smith, 1974). The curved surface of the rupture comprises an assembly of node-pairs along an internal boundary of the FEM problem domain. A vector of Green's Functions (GFs), for displacement due to slip along a fault, is calculated by predicting the displacement of GPS site positions caused by a unit dislocation for a given node-pair while simultaneously welding the remaining node-pairs. A matrix of GFs for the entire suite of m node-pairs is assembled by implementing an algorithm that systematically generates the unit dislocation and welding configurations over the rupture, executes the FEM, and extracts the predicted displacements caused by the dislocation of each node-pair.

A slip event induces relatively instantaneous incremental changes in stress and pore pressure and coseismic deformation is thus undrained. Therefore, the (undrained) coseismic deformation is calculated using the simplified elastic governing equations, having undrained values of Poisson's ratio substituted into the poroelastic portions of the problem domain. This is a useful result because m separate FEM calculations are required to assemble the matrix of GFs and the computation time for an elastic FEM is substantially lower than that of a coupled poroelastic FEM. The forward solution for elastic deformation due to a distribution of dislocating node-pairs is

$$\mathbf{G}m = d \tag{6}$$

where $\mathbf{G}$ is an matrix of GFs; $\boldsymbol{m}$ is a vector of dislocations; and $\boldsymbol{d}$ is a $1 \times n$ column vector of three-component displacements and/or displacement derivatives of the GPS site positions that can be time-

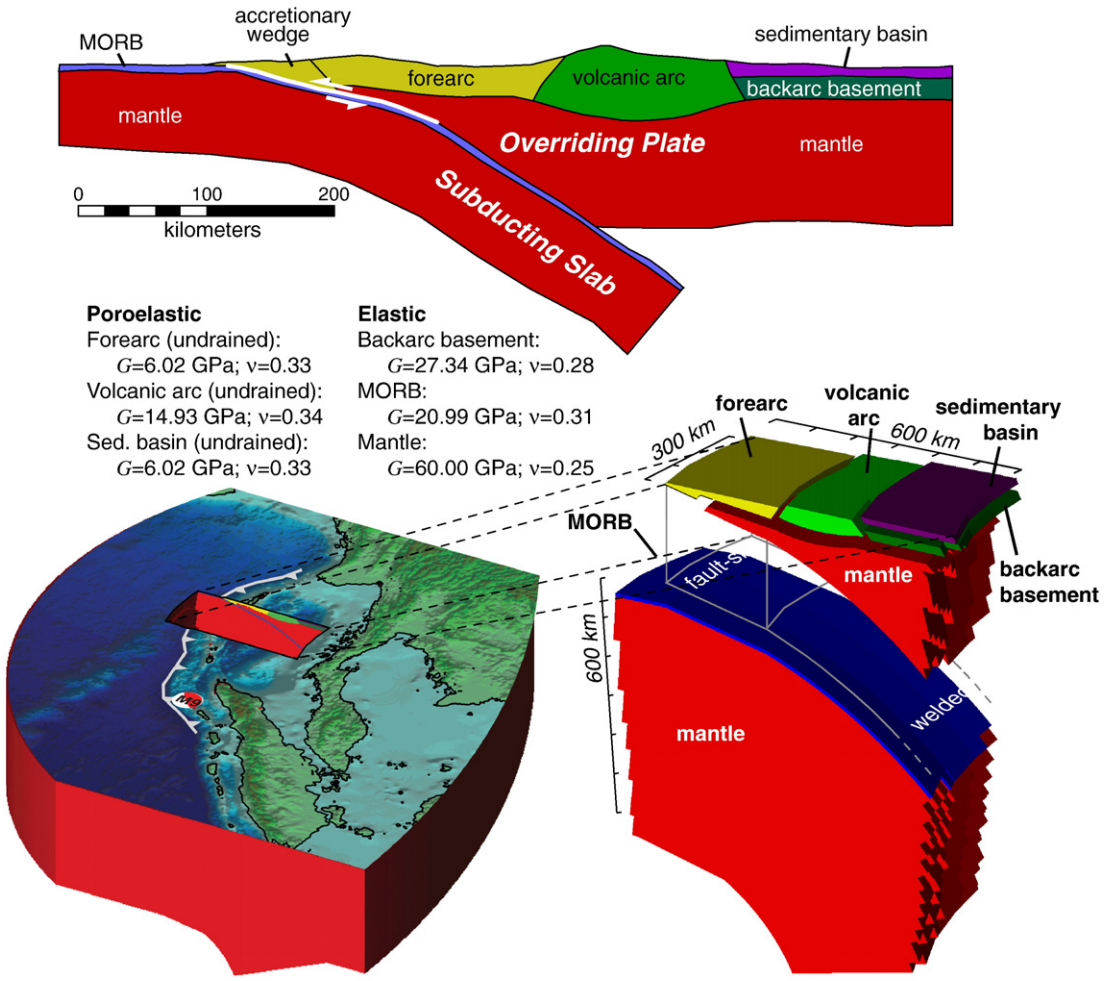

Fig. 2. Conceptual model and FEM configuration (adapted from Masterlark and Hughes (2008)). (a) Conceptual model. This 2D profile illustrates the geologic structure of the subduction zone. (b) FEM design and configuration. The 3D FEM is constructed by sweeping the 2D profile along the curvature of the Sunda Trench. The FEM comprises about 340,000 elements. The top of the problem domain is a free-surface. Lateral and bottom boundaries are zero displacement. The exploded view reveals the likeness of the FEM to the conceptual model.

dependent. For both down-dip (dd) and strike-slip (ss) dislocations, $\mathbf{G}=(\mathbf{G}_{dd}\mathbf{G}_{ss})$ and has dimensions of $2m\times n$. Similarly, the dislocation vector has dimensions $2\,m$ and $\boldsymbol{m}=(\boldsymbol{m}_{dd}\boldsymbol{m}_{ss})^{\mathrm{T}}$. Each coefficient $\boldsymbol{G}_{ij}$ represents the contribution to the displacement of $\boldsymbol{d}_j$ due to unit dislocation of node-pair $\boldsymbol{m}_i$. Most importantly, this matrix of FEM-generated GFs is readily calculated for inverse analyses of deformation data for dislocations embedded in an arbitrary domain (Masterlark, 2003; Masterlark and Hughes, 2008). Thus, FEMs permit us to simulate variable dislocations along fault surfaces embedded in a problem domain partitioned into the 3D rheologic configuration expected for the SASZ.

2.4. Inverse methods

We apply linear inverse methods to calibrate the slip distribution of the SAE, based on observed near-field displacement data from 34 GPS sites in the near-field region. These data are compiled from previous studies (Gahalaut et al., 2006; Subarya et al., 2006) and span northern Sumatra and the Nicobar and Andaman Islands (Table 1). We limit our study to near-field deformation data because the relative data importance (Menke, 1989) of far-field GPS sites (more than a fault-width from the rupture) is insignificant compared to that of GPS sites within the surface projection of the rupture for a megathrust event (Hutton et al., 2001). We partition the curved rupture surface, indicated by the distribution of aftershocks (Fig. 1), into a 25 (along-strike)×7 (down-dip) grid of quadrilateral slip patches. Each patch comprises four node-pairs sharing slip characteristics. We then recast Eq. (6) into a forward model that when inverted, simultaneously 1) Estimates the slip distribution that minimizes misfit to GPS data, 2) Imposes positive thrust and right-lateral strike-slip components, 3) Damps spurious solution oscillations, and 4) Accounts for the relative uncertainties of the GPS data. First, we pre-multiply Eq. (6) to account for the relative uncertainties of the data

$$\mathbf{W}\mathbf{G}m=\mathbf{W}d=\mathbf{G}_w m=d_w \tag{7}$$

where $\mathbf{W}$ is a diagonal data weighting matrix constructed from reported GPS measurement uncertainties, $\mathbf{W}_{ii}=1/\sigma_i$, (Table 1). Second, we reconfigure Eq. (7) using second-order Tikhonov regularization to damp the null space of the data kernel (Aster et al., 2005)

$$(\mathbf{G}_w^T\mathbf{G}_w+\beta^2\mathbf{L}^T\mathbf{L})m=\mathbf{G}_w^T d_w \text{ and } \mathbf{L}=\begin{pmatrix}\mathbf{L}_{dd} & 0\\ 0 & \mathbf{L}_{ss}\end{pmatrix} \tag{8}$$

where $\mathbf{L}$ is a $2m\times 2m$ matrix of coefficients for the finite difference approximation of the Laplacian operator for $\nabla^2\boldsymbol{m}=0$ over the 2D rupture surface. The down-dip and strike-slip sub-matrices of $\mathbf{L}$ are independent of one another but share the boundary condition specifications; along-strike and down-dip boundaries are set to Dirichlet (null) boundary conditions and the up-dip boundary is set to Neumann specifications ($\partial\boldsymbol{m}/\partial x=0$) (Fig. 3a) (Wang and

Table 1
Near-field GPS data.

Site	Lon, °E	Lat, °N	Displacement (m)			1σ (m)		
			East	North	Up	East	North	Up
(*Subarya et al., 2006*)								
bm12	98.9449	2.64259	−0.0890	−0.0198	−0.0805	0.0666	0.0238	0.0733
d962	97.4465	1.68602	−0.0332	−0.0270	−0.0535	0.0649	0.0253	0.0558
D972	96.6245	2.17441	0.0100	−0.0246	−0.5710	0.0669	0.0649	0.0669
Jahe	98.5075	3.14524	−0.2031	−0.0218	0.0053	0.1079	0.0882	0.0899
k504	95.2435	5.43378	−2.1140	−1.7634	−0.1717	0.1057	0.0882	0.0597
K505	95.2716	5.48000	−2.0675	−1.7455	−0.0611	0.1034	0.0873	0.0807
K515	95.4873	5.56851	−1.6599	−1.3420	−0.0462	0.0830	0.0671	0.0637
LANG	97.9999	4.42753	−0.3681	−0.0989	−0.0119	0.0411	0.0426	0.0608
LHOK	97.1585	5.08665	−0.5779	−0.2190	0.0765	0.0434	0.0478	0.1054
MART	98.6823	2.52419	−0.1448	−0.0127	−0.1228	0.0414	0.0240	0.0869
NIND	98.7506	2.72953	−0.1312	−0.0065	−0.4546	0.0326	0.0230	0.0916
PAND	98.8188	1.67586	−0.0411	−0.0355	−0.0264	0.0418	0.0397	0.0277
PIDI	95.9333	5.33080	−1.3993	−0.9557	0.0354	0.0405	0.0388	0.0490
PISU	99.1472	2.44756	−0.0825	−0.0143	−0.0129	0.0277	0.0311	0.0617
SIPA	99.0890	2.10263	−0.1027	−0.0586	−0.1144	0.0662	0.0631	0.0699
TIGA	98.5622	2.91856	−0.1426	−0.0041	0.0452	0.0228	0.0236	0.0305
R171	95.3877	2.95996	−3.8209	−4.3221	2.0988	0.0859	0.2161	0.0458
R173	95.5183	4.60702	−2.8537	−2.3763	−0.6010	0.1427	0.1188	0.0420
R174	95.3654	4.84193	−2.7719	−2.4143	−0.5838	0.1386	0.1200	0.0841
R175	95.2030	5.24116	−2.4349	−2.0761	−0.2266	0.1217	0.1038	0.1211
R176	95.0572	5.71287	−2.1745	−1.7109	−0.1421	0.1087	0.0855	0.0908
(*Gahalaut et al., 2006*)								
ABAY	93.0270	13.27800	−3.9000	−2.7100	0.4900	0.0400	0.0100	0.0500
EAST	93.0470	13.63100	−3.6200	−2.5100	0.9600	0.0400	0.0200	0.0700
LONG	92.9320	12.37600	−1.9600	−1.1000	−0.4800	0.0200	0.0100	0.0600
UGRH	92.7730	12.21600	−2.3900	−1.6600	−0.3600	0.0200	0.0100	0.0500
GOVI	92.9830	12.03600	−1.3600	−0.9500	−0.1800	0.0500	0.0200	0.0200
PBLR	92.7210	11.64900	−3.0700	−1.0300	−0.9600	0.0200	0.0100	0.0600
PASG	92.6760	11.17800	−2.9100	−1.1900	−0.7100	0.0200	0.0100	0.0500
HBAY	92.5690	10.69600	−3.2700	−2.6500	−0.2600	0.0100	0.0100	0.0200
CARN	92.8040	9.22500	−5.7600	−2.9500	−1.1100	0.0100	0.0100	0.0100
TERE	93.1240	8.30200	−5.8600	−3.0600	−2.8500	0.0200	0.0100	0.0400
KARD	93.5490	8.03600	−3.9700	−1.7200	−1.3500	0.0200	0.0100	0.0400
MERO	93.5410	7.51400	−4.9100	−2.8400	−2.1600	0.0200	0.0100	0.0500
CAMP	93.9340	7.00400	−4.1000	−2.3600	−1.6000	0.0200	0.0100	0.0300

Anderson, 1982). The regularization parameter β controls the tradeoff between minimizing misfit and satisfying the Laplacian operator. The least-squares solution to Eq. (8) is (Aster et al., 2005)

$$m = (\mathbf{G}_w^T\mathbf{G}_w + \beta^2\mathbf{L}^T\mathbf{L})^{-1}\mathbf{G}_w^T d_w. \quad (9)$$

We solve Eq. (9), subject to positivity constraints (Menke, 1989), while sweeping through β parameter space to find optimal solutions for $\boldsymbol{m}$. The positivity constraints require that solutions contain combinations of thrust and right-lateral strike-slip. These positivity constraints are different from Masterlark and Hughes (2008) where solutions were allowed to contain both thrust and normal components. In the absence of these constraints, solutions for $\boldsymbol{m}$ will include more oscillatory distributions having both normal and left-lateral slip regions that are not compatible with the focal mechanism (Fig. 1), even though these unconstrained solutions fit the GPS data better than their constrained counterparts.

3. Results

We wish to select a solution that gives a balance of misfit and smoothness. The generalized cross validation method (GCV) provides a means for selecting an optimal regularization parameter by minimizing the functional $V(\beta)$

$$V(\beta) = \frac{n\|\mathbf{G}_w m_\beta - d_w\|_2^2}{\mathrm{Trace}[\mathbf{I} - (\mathbf{G}_w^T\mathbf{G}_w + \beta^2\mathbf{L}^T\mathbf{L})^{-1}\mathbf{G}^T]^2} \quad (10)$$

where $\mathbf{I}$ is a $2m \times 2m$ identity matrix and $\boldsymbol{m}_\beta$ is the solution of Eq. (9) for a given regularization parameter (Aster et al., 2005). GCV results suggest $\beta^2 = 0.006$ is statistically the best solution (Fig. 3b). This slip distribution is rather rough and includes an unrealistic slip maximum of ≥100 m along the northeast edge of the rupture. Other investigators report similar problems of GCV results producing rough solutions and having slip magnitudes that are much too high (Freymueller et al., 1994). Alternatively, we can use the trade-off curve for roughness versus misfit (Gubbins, 2004) and a priori fault-slip constraints to identify a slip distribution that simultaneously minimizes roughness and misfit and has a maximum slip magnitude of about 30 m (Fig. 3c) in accord with other studies, as discussed below. This is our preferred solution.

Fault-slip is concentrated along the up-dip portion of the rupture that is west of northern Sumatra. A band of lower magnitude fault-slip occurs sub-parallel to the Sunda Trench and beneath the Nicobar and Andaman Islands (Fig. 4). This pattern is reasonably well resolved (Fig. 4b), based on the diagonal elements of the parameter resolution matrix, $\mathbf{R}_m$ (Aster et al., 2005)

$$\mathbf{R}_m = (\mathbf{G}_w^T\mathbf{G}_w + \beta^2\mathbf{L}^T\mathbf{L})^{-1}\mathbf{G}_w^T\mathbf{G}_w. \quad (11)$$

The small patch of significant slip at the northern edge of the rupture (Fig. 4a) is probably a numerical artifact, reflecting some aspect of the FEM that fails to adequately represent some unknown complexity in that region of the SASZ. Resolving this issue is the subject of ongoing analyses and beyond the scope of this study. Nonetheless, this misfit near the northern edge of the SAE rupture

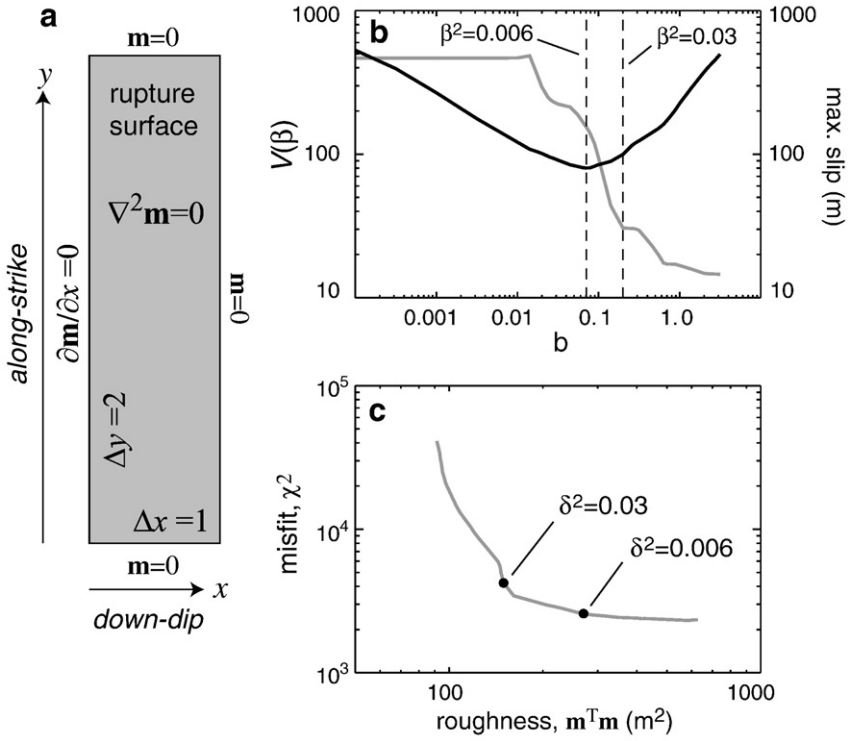

Fig. 3. Inverse methods. (a) Smoothing. A Laplacian operator is applied via finite-difference methods to smooth the estimated slip distribution. (b) GCV and maximum slip versus β. The optimal solution ($\beta^2=0.006$), according to GCV, includes an unrealistic fault-slip maximum of more than 100 m. (c) Tradeoff curve for roughness versus misfit. A value of $\beta^2=0.03$, our preferred solution, occurs at the knee of the curve. This solution produces a good balance of misfit and roughness, as well as a maximum fault-slip of about 30 m.

does not influence predictions for the southern portion of the SAE, the focus of this study. The pattern of shallow fault-slip, concentrated west of northern Sumatra, is consistent with seismological estimates (Ammon et al., 2005; Rhie et al., 2007) and tsunami-genesis results (Fujii and Satake, 2007; Grilli et al., 2007; Ioualalen et al., 2007). However, geodetic based analyses (Chlieh et al., 2007) place the majority of fault-slip near the Nicobar Islands.

Our calibrated slip distribution (Fig. 4a) is applied to a 3D FEM to predict the transient postseismic poroelastic deformation. In this FEM, the accretionary wedge, forearc, volcanic arc, and backarc sedimentary basin are poroelastic materials (Fig. 2). The oceanic crust capping the subducting slab is also poroelastic to a depth of 50 km, the maximum limit of rupture depth (Hyndman, 2007). The top (free surface) and lateral boundaries of the poroelastic materials are no-flow boundaries. The permeability of the poroelastic materials is $\kappa=10^{-16}$ m^2, an estimate for the bulk permeability of oceanic crust (Masterlark, 2003). The poroelastic properties of the oceanic crust are constrained by laboratory permeability experiments (Wang, 2000; Fisher, 1998) and seismological observations (Audet et al., 2009), and limited by the time interval between the two earthquakes (Fig. 5).

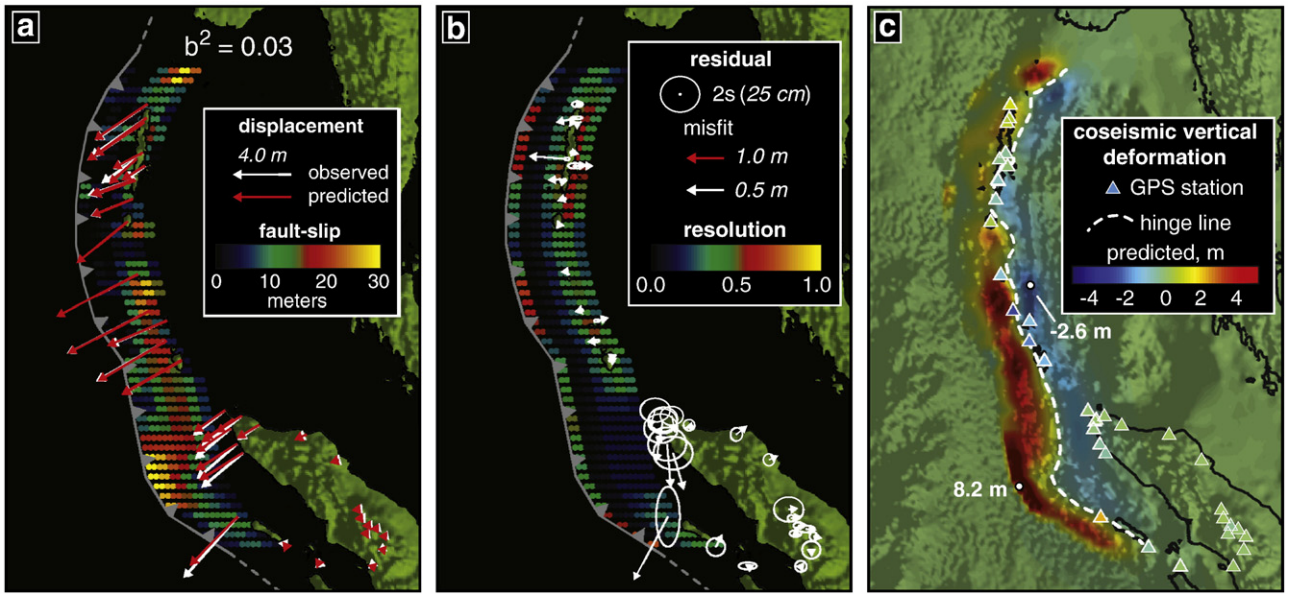

Fig. 4. Predicted slip and deformation of the SAE (adapted from Masterlark and Hughes (2008)). (a) Estimated fault-slip distribution and deformation predictions. (b) Parameter resolution and prediction misfit. (c) Vertical deformation. The predicted hinge line delimits zero vertical deformation and agrees with field observations (Meltzner et al., 2006).

Bulk permeability for the oceanic crust above 1×10^{-16} m^2 cannot account for the time delay between earthquakes due to rapid pore pressure re-equilibration, and bulk permeability below 1×10^{-17} m^2 is not geologically reasonable for cold, brittle subducting oceanic crust (Fisher, 1998; Christensen and Ramananantoandro, 1988). Additionally, the seismological observations of the Cascadian subduction zone indicate that the permeability contrast between the permeable oceanic crust and the overlying mantle wedge is more significant (1 to 4 orders of magnitude) than the actual bulk permeability assigned (Audet et al., 2009). We utilize an impermeable overlying plate on the time scale of the poroelastic model, which is geologically reasonable (Audet et al., 2009) due to the fact that the poroelastic effects occur within days to months. Audet et al. (2009) determined the interface of the seismogenic zone between the subducting oceanic crust and overlying plate to have a permeability of 5×10^{-25} to 5×10^{-22} m^2 which is much lower than the permeability of the actual oceanic crust. Including this permeability instead of a no flow boundary would not significantly change our results.

Our model simulates the relatively instantaneous coseismic poroelastic deformation and subsequent transient poroelastic deformation over the 90-day time interval between the SAE and NE. The coseismic distributions of deformation, stress, and pore pressure are initial conditions for the postseismic poroelastic deformation model. The uncertainties within these initial conditions rest on the assumptions of rheology, permeability, slip distribution, and boundary conditions of the FEM. We constrain these assumptions based on geological and seismological evidence for the SASZ (Barber et al., 2005; Kopp et al., 2002; Kopp and Kukowski, 2003; Pesicek et al., 2008). We ran multiple analyses of the FEM using varying permeability and rheology parameters and slip distributions. From these analyses, we deduce that the pore pressures range from 10^5 to 10^7. Furthermore, the sensitivity to the slip distribution was tested using an average slip of 15.25 m for each fault patch. We found that the postseismic poroelastic results of the FEM were robust and did not change our conclusions. Following the coseismic time step, pore pressures range from −1.4 to 1.6 MPa in the deep forearc (about 10 km depth) and −2.7 to 4.1 MPa in the subducting oceanic crust near the seismic barrier (Table 2 and Fig. 6a). Additionally, the coseismic slip introduces significant pore pressure changes in the subducting oceanic crust south of the SAE rupture, along the rupture surface of the NE, but prior to the NE. At the conclusion of the model (two days before the NE), pore pressures range from −0.5 to 0.4 MPa in the deep forearc and from −0.7 to 0.7 MPa in the subducting oceanic crust near the seismic barrier (Fig. 6c). The predicted postseismic increase in pore pressure near the NE hypocenter, and thus Coulomb stress, is two orders of magnitude greater than the minimal threshold, 10 kPa (Toda et al., 1998), believed to trigger slip.

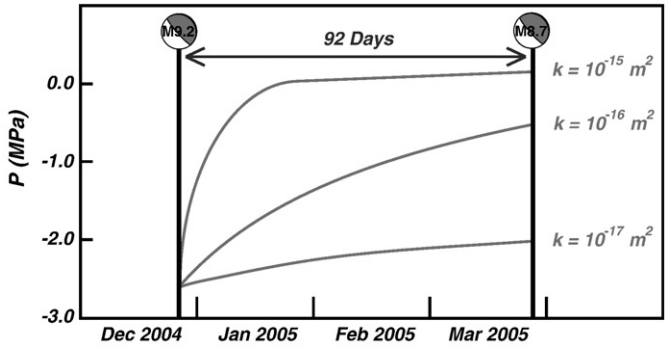

Fig. 5. Poroelastic stress-triggering due to the SAE. The poroelastic model allows for pore pressure recovery following the SAE. Various bulk permeabilities were examined for the subducting oceanic crust. A bulk permeability above 1×10^{-16} m^2 cannot account for the 90 day time interval between earthquakes. A bulk permeability below 1×10^{-17} m^2 has not been shown to be geologically reasonable (Wang, 2000; Fisher, 1998; Christensen and Ramananantoandro, 1988).

Table 2
Pore pressure maxima and minima.

Location	Time step	Near seismic barrier (MPa)		Whole model (MPa)	
		Max	Min	Max	Min
Forearc (4 °N/94 °E)	Beginning	1.6	−1.4	4.1	−3.6
Forearc (4 °N/94 °E)	End	0.4	−0.5	0.7	−1.4
Oceanic crust (2 °N/97 °E)	Beginning	4.1	−2.7	7.5	−4.4
Oceanic crust (2 °N/97 °E)	End	0.7	−0.7	2.0	−1.3

4. Discussion

Although we focus on pore pressure changes near the NE hypocenter, the range of pore pressure in the subducting oceanic crust increases when considering the whole model (Table 2). The absolute changes in pore pressure far from the seismic barrier are 4.1 MPa and 0.7 MPa for the coseismic (initial conditions) and 90-day time step, respectively. Absolute changes in pore pressure near the seismic barrier are −2.7 and −0.7 MPa for corresponding time steps. That is, the pore pressure near the hypocentral location of the NE increased by 2.0 MPa during the 3-month interval separating the SAE and NE (Fig. 5). These predictions suggest that the coseismic pore pressure distribution leads to a more persistent flow regime near the seismic barrier.

The pore pressures in the shallow forearc and volcanic arc recover relatively quickly within about a month of the coseismic rupture (Fig. 6b). In contrast, the pore pressure recovery in the subducting oceanic crust takes several months, even though the specified permeability is constant for all poroelastic materials in the FEM. Furthermore, the pore pressure changes in the subducting oceanic crust north of Sumatra recover more quickly than the maxima and minima near the seismic barrier. Since the specified permeability and pore fluid boundary conditions are constant for all poroelastic materials in the FEM, this variation in recovery time is due to the down-dip variation in slip over the rupture surface combined with the geometric configuration of the poroelastic oceanic crust near the down-dip limit of the rupture being “sandwiched” between relatively impermeable mantle of the underlying slab and overlying mantle wedge. That is, the geometric configuration of rheologic properties and boundary conditions can introduce multiple “apparent” deformation time constants even if the parameters that control the time dependence (e.g., permeability) are constant. This has implications for studies of postseismic deformation, for which it is customary to assign postseismic deformation mechanisms according to characteristic time constants of observed deformation epochs (Paul et al., 2007; Pollitz et al., 2006b).

The increase in pore pressure (2.0 MPa) southeast of the seismic barrier, and near the hypocentral location of the NE, translates to systematic increases in Coulomb stress (Eq. (1)) and thus the systematic decrease in fault stability following the SAE. We envision triggering of the SAE and NE in both space and time as a two step (impulse and response) process. First, the oceanic crust juxtaposed to the seismic barrier experiences an increase in Coulomb stress (McCloskey et al., 2005) and decrease in pore pressure (Fig. 6a) due to the coseismic rupture of the SAE (the impulse). Second, as time progresses fluids flow and re-equilibrate in response to the coseismic pore pressure gradients in the region of decreased pore pressure near the hypocentral location of the NE (the response). Following the SAE, fluids migrate from regions of high pore pressure to regions of low pore pressure. In this flow regime, fluids migrate both up-dip and down-dip to the edge of the seismogenic zone, as well as laterally (along-strike) within the subducting oceanic crust. This lateral migration of fluids within the subducting oceanic crust occurs along the rupture zone of the SAE, as well as through the seismic barrier to

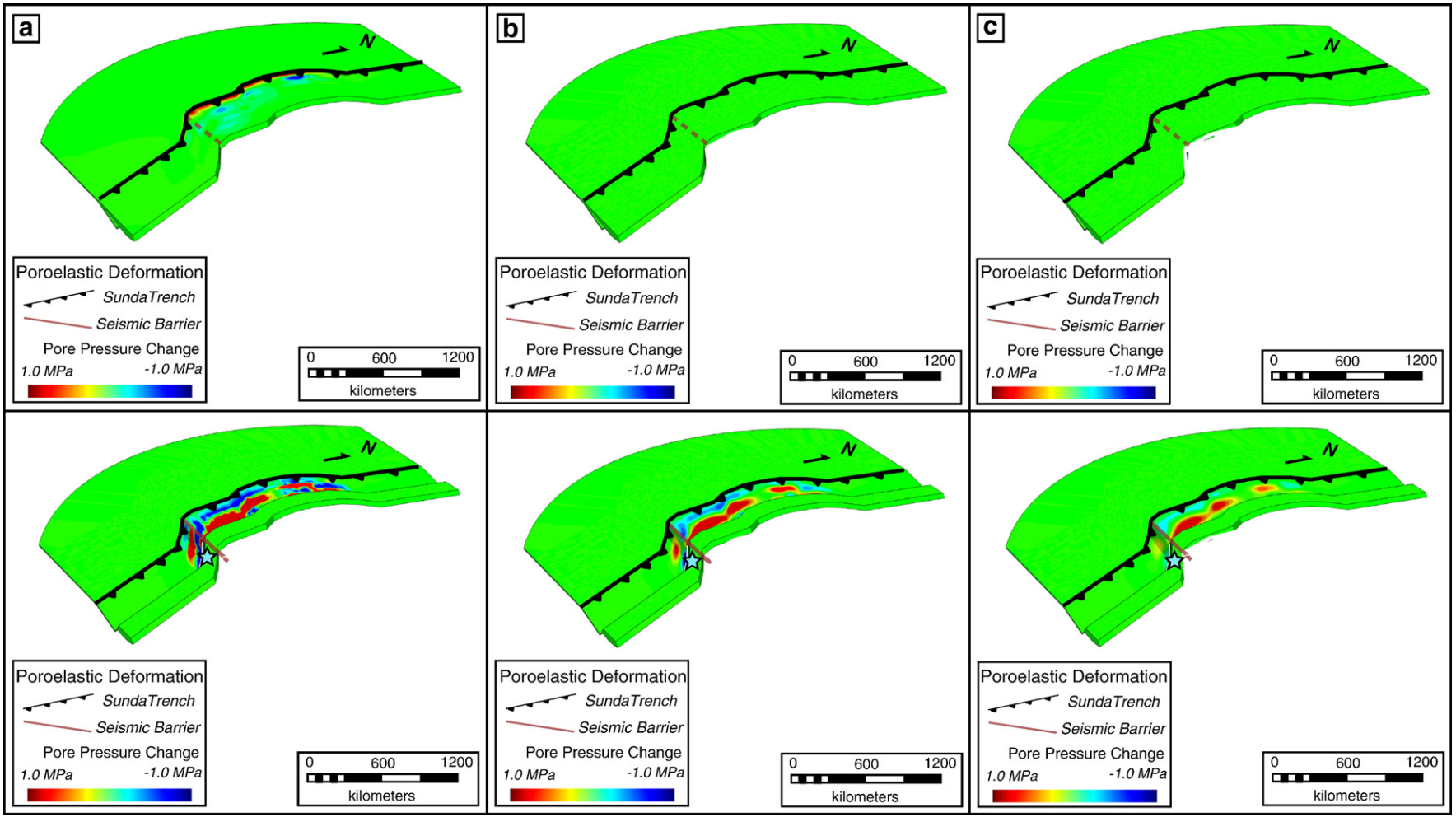

Fig. 6. Pore pressure recovery following the SAE. (a) First time segment (coseismic poroelastic deformation). (b) Middle time segment (45 days after coseismic dynamic rupture). (c) Last time segment (two days before Nias earthquake). Red solid or dashed line represents location of the seismic barrier in the subducting oceanic crust. Teal star represents NE hypocentral location. Top row of images includes forearc poroelastic deformation. In the bottom row of images the forearc has been stripped away to view the subducting oceanic crust.

the south of the SAE rupture near the NE hypocenter. Thus, poroelastic effects may correspond to increasing changes in Coulomb stress due to slow re-equilibration and lateral migration of pore fluids within the subducting oceanic crust. Lateral migration of fluids demonstrated here has also been proposed to account for migration of slow slip events in subduction zones elsewhere (Melbourne et al., 2005).

The predicted increase in pore pressure (2.0 MPa) for the NE hypocentral region directly correlates to positive changes in Coulomb stress (Eq. (1)) that are two orders of magnitude greater than corresponding Coulomb stress increases predicted for viscoelastic models of postseismic deformation (Pollitz et al., 2006a). Furthermore, the timing of postseismic poroelastic relaxation near the NE hypocenter is consistent with the three-month interval separating the SAE and NE. Therefore, the predicted coseismic distribution of pore pressure for the SAE and timing of postseismic poroelastic relaxation produce Coulomb stress changes of sufficient magnitude to account for both the spatial and temporal proximity of the SAE and NE.

The stress released by the coseismic fault-slip propagates into the region surrounding the fault. The response of the near-field region to this stress depends on the rheologic partitioning. There are three mechanisms (all of which have been demonstrated in laboratory and field measurements) that contribute to postseismic deformation — afterslip, viscoelastic relaxation, and poroelastic relaxation. Additionally, interseismic strain accumulation continues during all stages of the earthquake cycle, except during the relatively instantaneous coseismic slip. Considering the sheer size of the SAE, contributions from all three postseismic deformation mechanisms are expected to be significant. Previous studies calibrate the afterslip and viscoelastic relaxation parameters to near-field GPS measurements (Chlieh et al., 2007; Paul et al., 2007).

Poroelastic deformation is not considered because the other two mechanisms dominate the measured near-field postseismic deformation. Comparatively speaking, the expected magnitude of viscoelastic deformation is expected to be five times greater than that of the poroelastic deformation for the SAE (Fig. 7). A similar dominance of viscoelastic (compared to poroelastic) postseismic deformation was predicted for other subduction zone earthquakes (Masterlark et al., 2001). Nonetheless, the predicted poroelastic deformation is expected to be a significant contributor to the observed GPS measurements, particularly for the vertical deformation of the Nicobar Islands and the islands west of northern Sumatra (Fig. 7). In contrast to the dominance of viscoelastic postseismic deformation, the poroelastic contribution to postseismic Coulomb stress changes near the NE hypocenter is much greater than that of the corresponding viscoelastic contribution. This suggests that postseismic poroelastic effects are important, particularly for earthquake stress-triggering analyses.

We propose treating the predicted poroelastic deformation as a correction to postseismic deformation data, as is customary for predicted interseismic strain accumulation. This addresses the bias inherent to interpretations that are based on a single mechanism and neglect the other contributions. For example, the rheologic (viscosity) structure proposed by Pollitz et al. (2006a) to account for postseismic deformation of the SAE does not require any afterslip. Alternatively, the afterslip distribution proposed by Hashimoto et al. (2006) to account for this same deformation does not require any viscoelastic relaxation. Such studies based on a single postseismic deformation mechanism introduce unknown bias and suppress the reliability of interpretations and predictions. Compared to afterslip and viscoelastic relaxation, the poroelastic deformation will most certainly not explain a large portion of the observed postseismic deformation. In fact, the character of poroelastic deformation may be contrary to some displacement observations (e.g., Paul et al., 2007). If we then rule out poroelastic deformation altogether in favor of some other mechanism (say afterslip, which has many more adjustable parameters), we are assuming that either fluids are not present in the crust or that poroelastic behavior is insignificant. However, fluids are

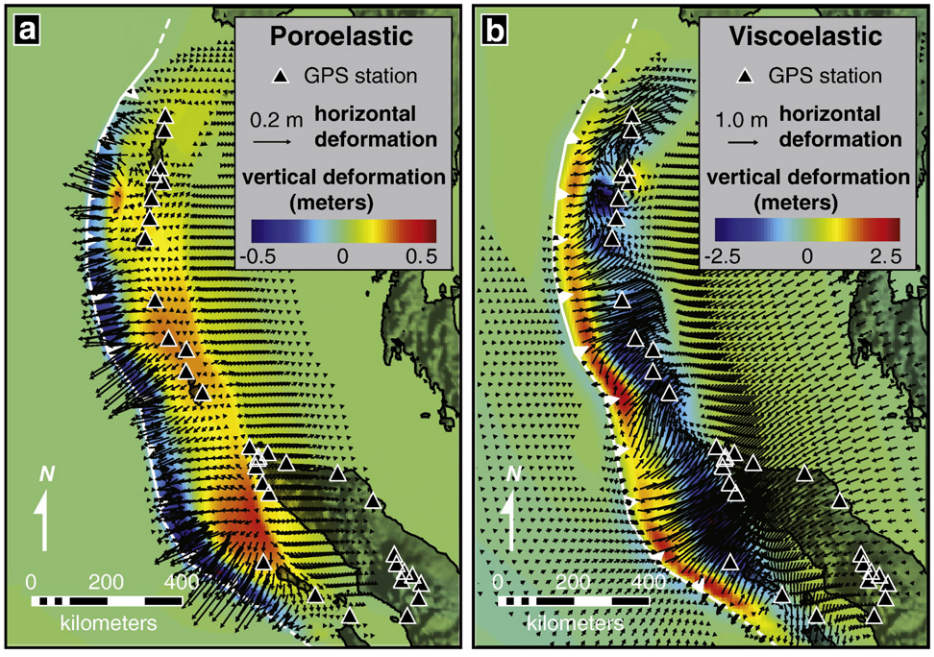

Fig. 7. Predicted poroelastic and viscoelastic deformation of the SAE. The slip model of Masterlark and Hughes (2008) drives the FEM shown in Fig. 2. Colors and arrows represent vertical and horizontal deformation, respectively, with respect to the coseismic deformation field. Arrows are not plotted for predicted horizontal displacements less than 1 cm. (a) Poroelastic deformation. Postseismic poroelastic deformation is complete several months after the SAE. Measurable poroelastic deformation is primarily limited to the surface projection of the rupture, due to the distribution of coseismic slip and geometric configuration of rheologic properties. The horizontal deformation is maximum (a few tens-of-centimeters) where the coseismic nodal plane intersects the land surface. Unfortunately, this region of predicted maximum horizontal poroelastic deformation is offshore and no GPS sites are available to verify the predictions. However, substantial poroelastic uplift is predicted for the Nicobar Islands. (b) Viscoelastic deformation. Viscoelastic relaxation is calculated for a period of 10 years following the SAE ($\mu = 10^{18}$ Pa s). Magnitudes of viscoelastic deformation are about 5 times greater than those of poroelastic relaxation. However, the direction of displacements differs for the different deformation mechanisms.

present in the crust (e.g., Nur and Walder, 1990, and references therein) and their presence and significance in an accretionary prism are clear (e.g., Moore et al., 2007). Furthermore, as demonstrated here, poroelastic contributions are significant for explaining the delayed triggering of the NE due to the SAE.

5. Conclusions

We present a quantitative analysis of poroelastic deformation of the SAE and stress-triggering of the NE. We estimate the slip distribution for the SAE from near-field GPS data using linear inverse methods and FEM-generated Green's Functions, which account for the distribution of material properties of the SASZ. The estimated slip distribution then drives a forward model that simulates poroelastic processes induced by the SAE. The poroelastic structure of the SASZ produces two flow regimes having two separate time constants. Pore pressure, and thus poroelastic deformation, decays rapidly (~1 month) in the shallow forearc and volcanic arc of the overriding plate. This relatively rapid recovery in pore pressure may help to explain the timing and location of near-field aftershock swarms (Fig. 1) (Piombo et al., 2005). The timing for pore pressure recovery is more sluggish (several months) in the oceanic crust of the down-going slab due, in part, to the geometric configuration of the poroelastic oceanic crust being "sandwiched" between relatively impermeable mantle of the underlying slab and overlying mantle wedge (Audet et al., 2009). In particular, the pore pressure southeast of the seismic barrier and near the hypocenter of the NE slowly, but systematically, recovers during the three-month interval separating the SAE and NE. This suggests that transient pore pressure contributes significantly to the spatial and temporal proximity of these two events.

A complete explanation of stress-triggering initiated by the SAE must include poroelastic effects. It is well-known that a transient pore pressure pulse can trigger transient seismicity (Raleigh et al., 1976) and changes in pore pressure in this study and previous studies have been shown to contribute to changes in Coulomb stress at the same magnitude as normal and shear stresses (Eq. (1)) (e.g., 2001 M7.6 Bhuj earthquake, 1995 M8 Jalisco, Mexico earthquake, and 1992 M7.3 Landers earthquakes) (Bosl and Nur, 2002; Gahalaut et al., 2008; Masterlark, 2003; Masterlark and Wang, 2000; Masterlark and Wang, 2002). By extension, if pore pressure is an important contributor to analyses of stress-triggering, then poroelastic deformation should not be neglected from postseismic deformation analyses, even if other postseismic deformation mechanisms dominate the deformation signal. The FEM-based techniques presented here allow for simulating the evolution of coseismic and postseismic deformation, stress, and pore pressure due to megathrust earthquakes in subduction zones having complex geometric configurations of rheologic properties.

Acknowledgements

This work is supported in part by NASA under award NNX060F10G, NSF Geophysics award EAR-0911466, and the W. Gary Hooks Endowed Geology Fund. Academic licensing and technical support for Abaqus software is provided by Simulia Inc., Dassault Systèmes. We thank Fred F. Pollitz for insightful comments and Thorne Lay and Lars P. Stixrude for astute reviews.

References

Ammon, C.J., Ji, C., Thio, H.K., Robinson, D., Ni, S., Hjorleifsdottir, V., Kanamori, H., Lay, T., Das, S., Helmberger, D., Ichinose, G., Polet, J., Wald, D., 2005. Rupture process of the 2004 Sumatra–Andaman Earthquake. Science 308, 1133–1139.

Aster, R.C., Borchers, B., Thurber, C.H., 2005. Parameter Estimation and Inverse Problems. Elsevier Academic Press, San Diego.

Audet, P., Bostock, M.G., Christensen, N.I., Peacock, S.M., 2009. Seismic evidence for overpressured subducted oceanic crust and megathrust fault sealing. Nature 457, 76–78.

Banerjee, P., Pollitz, F., Nagarajan, B., Bürgmann, R., 2007. Coseismic slip distributions of the 26 December 2004 Sumatra–Andaman and 28 March 2005 Nias earthquakes from GPS static offsets. Bull. Seismol. Soc. Am. 97, S86–S102.

Barber, A.J., Crow, M.J., Milsom, J.S., 2005. Sumatra. Geology, Resources and Tectonic Evolution, Memoir no. 31. Geological Society, London.

Beeler, N.M., Simpson, R.W., Hickman, S.H., Lockner, D.A., 2000. Pore fluid pressure, apparent friction, and Coulomb failure. J. Geo. Res. 105, 25533–25542.

Bilek, S.L., 2007. Using earthquake source durations along the Sumatra–Andaman subduction system to examine fault-zone variations. Bull. Seismol. Soc. Am. 97, S62–S70.

Bird, P., 2003. An updated digital model of plate boundaries. G-Cubed 4.

Bosl, W.J., Nur, A., 2002. Aftershocks and pore fluid diffusion following the 1992 Landers earthquake. J. Geo. Res. 107.

Byerlee, J., 1978. Friction of rocks. P. A. Geoph. 116, 615–626.

Chlieh, M., Avouac, J.-P., Hjorleifsdottir, V., Song, T.-R.A., Ji, C., Sieh, K., Sladen, A., Hebert, H., Prawirodirdjo, L., Bock, Y., Galetzka, J., 2007. Coseismic slip and afterslip of the great M_w 9.15 Sumatra–Andaman earthquake of 2004. Bull. Seismol. Soc. Am. 97, S152–S173.

Christensen, N.I., Ramananantoandro, R., 1988. Permeability of the oceanic crust based on experimental studies of basalt permeability at elevated pressures. Tectonophysics 149, 181–186.

Cocco, M., Rice, J.R., 2002. Pore pressure and poroelasticity effects in Coulomb stress analysis of earthquake interactions. J. Geo. Res. 107.

Cocco, M., Rice, J.R., 2003. Corrections to "Pore pressure and poroelasticity effects in Coulomb stress analysis of earthquake interactions. J. Geo. Res. 108.

Engdahl, E.R., Villaseñor, A., DeShon, H.R., Thurber, C.H., 2007. Bull. Seismol. Soc. Am. 97, S43–S61.

Fisher, A.T., 1998. Permeability within basaltic oceanic crust. Rev. Geophys. 36, 143–182.

Freymueller, J., King, N.E., Segall, P., 1994. The Co-seismic slip distribution of the Landers earthquake. Bull. Seismol. Soc. Am. 84, 646–659.

Fujii, Y., Satake, K., 2007. Tsunami source of the 2004 Sumatra–Andaman earthquake inferred from tide gauge and satellite data. Bull. Seismol. Soc. Am. 97, S192–S207.

Gahalaut, V.K., Kalpna, 2005. 28 March 2005 Sumatra earthquake: expected, triggered, or aftershock? Cur. Sci. 89, 452–454.

Gahalaut, V.K., Nagarajan, B., Catherine, J.K., Kumar, S., 2006. Constraints on 2004 Sumatra–Andaman earthquake rupture from GPS measurements in Andaman–Nicobar Islands. EPSL 242, 365–374.

Gahalaut, K., Gahalaut, V.K., Kayal, J.R., 2008. Poroelastic relaxation and aftershocks of the 2001 Bhuj earthquake, India. Tectonophysics 460, 76–82.

Grilli, S.T., Ioualalen, M., Asavanant, J., Shi, F., Kirby, J., Watts, P., 2007. Source constraints and model simulation of the December 26, 2004 Indian Ocean tsunami. J. Waterway Port Coastal Ocean Eng. 133, 414–428.

Gubbins, D., 2004. Time Series Analysis and Inverse Theory for Geophysicists. Cambridge University Press, Cambridge.

Gutscher, M.-A., Malavieille, J., Lallemand, S., Collet, J.-Y., 1999. Tectonic segmentation of the Northern Andean margin: impact of the Carnegie Ridge collision. EPSL 168, 255–270.

Hashimoto, M., Choosakul, N., Hashizime, M., Takemoto, S., Takiguchi, H., Fukuda, Y., Fujimori, K., 2006. Crustal deformations associated with the great Sumatra–Andaman earthquake deduced from continuous GPS observation. Ear Plan Space 58, 127–139.

Hsu, Y.-J., Simons, M., Avouac, J.-P., Galetzka, J., Sieh, K., Chlieh, M., Natawidjaja, D., Prawirodirdjo, L., Bock, Y., 2006. Frictional afterslip following the 2005 Nias–Simeulue earthquake, Sumatra. Science 312, 1921–1926.

Hughes, K.L.H., Masterlark, T., 2008. Slip distribution for the 2004 Sumatra–Andaman earthquake constrained by both GPS data and tsunami run-up measurements. Boll. Geo. Teor. App. 49.

Hutton, W., DeMets, C., Sánchez, O., Suárez, G., Stock, J., 2001. Slip kinematics and dynamics during and after the 1995 October 9 Mw = 8.0 Colima-Jalisco earthquake, Mexico, from GPS geodetic constraints. Geophysical Journal International 146, 637–658.

Hyndman, R.D., 2007. The seismogenic zone of subduction thrust faults: what we know and what we don't know. In: Dixon, T.H., Moore, J.C. (Eds.), The Seismogenic Zone of Subduction Thrust Faults. Columbia University Press, New York, pp. 15–40.

Ioualalen, M., Asavanant, J., Kaewbanjak, N., Grilli, S.T., Kirby, J.T., Watts, P., 2007. Modeling the 26th December 2004 Indian Ocean tsunami: case study of impact in Thailand. J. Geo. Res. 112.

Kieckhefer, R.M., Shor Jr., G.G., Curray, J.R., 1980. Seismic refraction studies of the Sunda Trench and forearc basin. J. Geo. Res. 85, 863–889.

King, G.C.P., Stein, R.S., Lin, J., 1994. Static stress changes and the triggering of earthquakes. Bull. Seismol. Soc. Am. 84, 935–953.

Kopp, H., Kukowski, N., 2003. Backstop geometry and accretionary mechanics of the Sunda margin. Tectonics 22.

Kopp, H., Klaeschen, D., Flueh, E.R., Bialas, J., Reichert, C., 2002. Crustal structure of the Java margin from seismic wide-angle and multichannel reflection data. J. Geo. Res. 107.

Masterlark, T., 2003. Finite element model predictions of static deformation from dislocation sources in a subduction zone: sensitivities to homogeneous, isotropic, Poisson-solid, and half-space assumptions. J. Geo. Res. 108.

Masterlark, T., Hughes, K.L.H., 2008. Next generation of deformation models for the 2004 M9 Sumatra–Andaman earthquake. Geo. Res. Let. 35.

Masterlark, T., Wang, H.F., 2000. Poroelastic coupling between the 1992 Landers and Big Bear earthquakes. Geo. Res. Let. 27, 3647–3650.

Masterlark, T., Wang, H.F., 2002. Transient stress-coupling between the 1992 Landers and 1999 Hector Mine earthquakes. Bull. Seismol. Soc. Am. 92, 1470–1486.

Masterlark, T., DeMets, C., Wang, H.F., Sánchez, O., Stock, J., 2001. Homogeneous vs heterogeneous subduction zone models: Coseismic and postseismic deformation. Geophysical Research Letters 28, 4047–4050.
McCloskey, J., Nalbant, S.S., Steacy, S., 2005. Indonesian earthquake: earthquake risk from co-seismic stress. Nature 434, 291.
Melbourne, T.I., Szeliga, W.M., Miller, M.M., Santillan, V.M., 2005. Extent and duration of the 2003 Cascadia slow earthquake. Geo. Res. Let. 32.
Melosh, H.J., Raefsky, A., 1981. A simple and efficient method for introducing faults into finite element computations. Bull. Seismol. Soc. Am. 71, 1391–1400.
Meltzner, A.J., Sieh, K., Abrams, M., Agnew, D.C., Hudnut, K.W., Avouac, J.-P., Natawidjaja, D.H., 2006. Uplift and subsidence associated with the great Aceh–Andaman earthquake of 2004. J. Geo. Res. 111.
Menke, W., 1989. Geophysical Data Analysis: Discrete Inverse Theory, International Geophysical Series, vol. 45. Academic Press, Inc.
Mignan, A., King, G., Bowman, D., Lacassin, R., Dmowska, R., 2006. Seismic activity in the Sumatra–Java region prior to the December 26, 2004 ($M_w = 9.0$–9.3) and March 28, 2005 ($M_w = 8.7$) earthquakes. EPSL 244, 639–654.
Moore, G.F., Bangs, N.L., Taira, A., Kuramoto, S., Pangborn, E., Tobin, H.J., 2007. Three dimensional splay fault geometry and implications for tsunami generation. Science 318, 1128–1131.
Nur, A., Walder, J., 1990. Time-dependent hydraulics of the Earth's crust. In: National Research Council (Ed.), The Role of Fluids in Crustal Processes. National Academy Press, Washington, D.C., pp. 113–127.
Okada, T., 1992. Internal deformation due to shear and tensile faults in a half-space. Bulletin of the Seismological Society of America 82, 1018–1040.
Paul, J., Lowry, A.R., Bilham, R., Sen, S., Smalley Jr., R., 2007. Postseismic deformation of the Andaman Islands following the 26 December, 2004 Great Sumatra–Andaman earthquake. Geo. Res. Let. 34.
Pesicek, J.D., Thurber, C.H., Widiyantoro, S., Engdahl, E.R., DeShon, H.R., 2008. Complex slab subduction beneath northern Sumatra. Geo. Res. Let. 35.
Piombo, A., Martinelli, G., Dragoni, M., 2005. Post-seismic fluid flow and Coulomb stress changes in a poroelastic medium. Geo. J. Int. 162, 507–515.
Plafker, G., Savage, J.C., 1970. Mechanism of the Chilean earthquakes of May 21 and 22, 1960. Bull. Geo. Soc. Am. 81, 1001–1030.
Pollitz, F.F., Banerjee, P., Bürgmann, R., Hashimoto, M., Choosakul, N., 2006a. Stress changes along the Sunda trench following the 26 December 2004 Sumatra–Andaman and 28 March 2005 Nias earthquakes. Geo. Res. Let. 33.
Pollitz, F.F., Bürgmann, R., Banerjee, P., 2006b. Post-seismic relaxation following the great 2004 Sumatra–Andaman earthquake on a compressible self-gravitating Earth. Geo. J. Int. 167, 397–420.
Raleigh, C.B., Healy, J.H., Bredehoeft, J.D., 1976. An experiment in earthquake control at Rangely, Colorado. Science 191, 1230–1237.
Rhie, J., Dreger, D., Burgmann, R., Romanowicz, B., 2007. Slip of the 2004 Sumatra–Andaman earthquake from joint inversion of long-period global seismic waveforms and GPS static offsets. Bull. Seismol. Soc. Am. 97, S115–S127.
Ruff, L.J., 1996. Large earthquakes in subduction zones: segment interaction and recurrence times. In: Bebout, G.E., Scholl, D.W., Kirby, S.H., Platt, J.P. (Eds.), Subduction: Top to Bottom. American Geophysical Union, Washington, D.C., pp. 91–104.
Smith, Jr., A.T., 1974. Time-dependent strain accumulation and release at island arcs: Implications for the 1946 Nankido earthquake. Ph.D. Thesis, MIT.
Stein, R.S., 1999. The role of stress transfer in earthquake occurrence. Nature 402, 605–609.
Stein, S., Okal, E.A., 2005. Speed and size of the Sumatra earthquake. Nature 434, 581–582.
Subarya, C., Chlieh, M., Prawirodirdjo, L., Avouac, J.-P., Bock, Y., Sieh, K., Meltzner, A.J., Natawidjaja, D.H., McCaffrey, R., 2006. Plate-boundary deformation associated with the great Sumatra–Andaman earthquake. Nature 440, 46–51.
Toda, S., Stein, R.S., Reasenberg, P.A., Dieterich, J.H., Yoshida, A., 1998. Stress transferred by the 1995 $M_w = 6.9$ Kobe, Japan, shock: effect on aftershocks and future earthquake probabilities. J. Geo. Res. 103, 24543–24565.
Turcotte, D.L., Schubert, G.J., 2002. Geodynamics: Applications of Continuum Physics to Geological Problems, second ed. Cambridge University Press, New York.
Vigny, C., Simons, W.J.F., Abu, S., Bamphenyu, R., Satirapod, C., Choosakul, N., Subarya, C., Socquet, A., Omar, K., Abidin, H.A., Ambrosius, B.A.C., 2005. Insight into the 2004 Sumatra–Andaman earthquake from GPS measurements in Southeast Asia. Nature 436, 201–206.
Wang, H.F., 2000. Theory of Linear Poroelasticity: With Applications to Geomechanics. Princeton University Press, Princeton.
Wang, H.F., Anderson, M.P., 1982. Introduction to Groundwater Modeling: Finite Difference and Finite Element Methods. Academic Press, San Diego.